ngVLA Dynamic Range

W. D. Cotton and J. J. Condon October 26, 2017

***Abstract*—The ngVLA is required to produce images over a 100:1 range of angular resolution at a single wavelength using a fixed configuration, so it cannot have a scale-free power-law radial distribution of antennas. The strawman configuration has three scales: (1) 114 antennas are in the dense central core of radius ~ 1 km, and the remaining 100 antennas lie near (2) the three 20 km arms of the VLA A configuration or (3) highways up to ~ 200 km from the core. Thus its naturally weighted PSF or "dirty beam" has three angular scales: (1) a narrow central spike, (2) a shoulder $\sim 10\times$ wider, and (3) a high pedestal $\sim 100\times$ wider that contains most of the beam solid angle. The desired elliptical Gaussian dirty beam can be approximated only by heavily reweighting baselines of different lengths.**

This memo analyzes the dirty beams of three antenna configurations proposed for the ngVLA and their effects on the dynamic range and sensitivity achievable for a deep 3 GHz point-source survey made with $\sim 0\farcs5$ resolution. Our simulations used a real VLA S band "quiet" sky model and models with stronger point sources added. The effects of strong sources, pixelization, and calibration/pointing errors were included. Relatively harsh Briggs robust weighting plus outer and inner tapers on the (u, v) distribution were needed to produce better-behaved PSFs. Even with calibration errors, the strawman configuration did not degrade the dynamic range of the quiet images at the level tested (DR ≈3000:1). Adding stronger sources did limit the dynamic range to $\lesssim 4 \times 10^5$:1, and to $\lesssim 0.9 \times 10^5$:1 for larger calibration errors. It was necessary to "AutoCenter" strong point sources on facet pixels, but even that was of limited help as the calibration errors increased. Two modifications of the strawman design were considered. Dithering antenna locations about the VLA arms improved snapshot (u, v) coverage but made little difference to extended syntheses. The "triangular" configuration increased dynamic range by 30% in the tests performed. The reweightings required to achieve even marginally acceptable dirty beams lower ngVLA sensitivity by factors $F \sim 2.5$.

***Index Terms*—interferometry, dynamic range**

I. Introduction

THE most unique technical requirement for the ngVLA [1] is the ability to produce images over a 100:1 range of angular resolution at a single wavelength using a fixed configuration of 214 antennas. In contrast, the reconfigurable VLA achieves its ∼30:1 resolution range by having four antenna configurations separated by factors of $10^{1/2}$ in size, so each configuration needs to cover only a $10^{1/2}$:1 resolution range.

Each VLA configuration has a scale-free power-law distribution of antenna distances from the array center for a smooth radial (u, v)-plane coverage. Earth-rotation synthesis VLA images made with nearly natural weighting have good "dirty" beams characterized by an elliptical, nearly Gaussian main lobe and low sidelobe levels. A similar power-law distribution for an ngVLA configuration with 100:1 resolution coverage would leave few antennas in the central "core" of radius ~ 1 km. Many ngVLA key science goals [2] require a compact core sensitive to low-brightness emission, so 114 of the 214 antennas have been placed in the dense core of the strawman ngVLA. For practical reasons, the remaining ngVLA antennas are distributed on two larger scales: (1) along the three 20 km arms the VLA A configuration and (2) scattered over a region ~ 200 km in radius. The naturally weighted dirty beam of the full ngVLA ([3], Figure 1) reflects these three scales, with a narrow central spike, a shoulder $\sim 10\times$ as wide as the spike, and a conical pedestal about $100\times$ as wide. The mean attenuation factor of the pedestal is ~ 0.1, so most of the dirty-beam power is in the pedestal, not the spike or the shoulder. Moderate Briggs weighting (robust parameter $R = -0.2$) yields only a slight improvement on this unacceptably dirty beam. Increasing the beamwidth by tapering away the longer baselines gradually yields better dirty beams, but low sidelobe levels can be achieved only by tapering heavily enough to suppress all baselines longer than the core diameters ([3], Figure 2).

The fixed configuration and its limitations represent the largest technical risk to the ngVLA project, larger than the risks associated with the individual antenna and receiver designs, which have evolved continuously since the VLA was designed nearly a half century ago. Important questions remain: How much can the dirty beam be improved by sophisticated weighting and tapering in the (u, v) plane? How much sensitivity will be sacrificed in the process? For which science cases will ngVLA images be limited by dynamic range, and not by thermal noise?

High dynamic range is most important low frequencies, where there are many sources in a given field of view, and some may be substantially brighter that the target(s) of interest. A number of factors determine the attainable dynamic range, defined here as the ratio of the brightest source in the field to the off-source rms in the image. (An alternative definition more appropriate to source surveys would be the ratio of the quadratic sum of flux densities in the field to the off-source rms in the image.) These factors include the antenna pointing and gain calibration stability, but most are related to the (u, v)-plane coverage and its Fourier transform, the point-spread-function PSF or "dirty beam." In particular, most image artifacts are proportional to the amplitude and extent of the PSF sidelobes. Smooth, quasi-random, and dense (u, v) coverage leads to elliptical Gaussian beams with low sidelobes while clumpy, linear, and sparse coverage leads to deformed beams with high sidelobes.

This memo examines the quality of the PSF and its effect on dynamic range for a deep 3 GHz (S band) point-source survey by the strawman ngVLA configuration and two possible

National Radio Astronomy Observatory, 520 Edgemont Rd., Charlottesville, VA, 22903 USA email: bcotton@nrao.edu

modifications. Tests using the Obit package [4] [1] on simulated data are presented.

II. Central Condensation

The proposed ngVLA is a compromise optimized for science requiring either high angular resolution or high surface-brightness sensitivity at low resolution, so about half of the antennas must lie in a compact core supplemented by outlying antennas for higher resolution. The most recent (September 2017) ngVLA strawman design has 114 antennas in the core $r \sim 1$ km core plus 100 more providing baselines up to several hundred km. The large-scale ngVLA configuration is especially critical because there is a very large number of nearly equivalent baselines from each of the remote antennas to each antenna in the core. In the limit of natural weighting, the ngVLA can be approximated by a large central "single dish" with 100 baselines from the outlying antennas to the central core. For $\sim 1''$ resolution at $\lambda = 10$ cm wavelength, only 80 to 90 of the outlying antennas are useful. Uniform or Briggs robust weighting will increase the effective number of baselines above 80–100 and reduce the sidelobe levels, but at a significant cost in sensitivity, so the configuration of the several hundred effective baselines needs to be chosen with care.

III. The ngVLA Strawman Configuration

The best way to view an antenna configuration is by the snapshot (u, v)-plane coverage. The instantaneous coverage for a source at 60° declination interior to $600,000\lambda$ at $\lambda = 10$ cm ($\nu = 3$ GHz) is shown in Figure 1 Left. Figure 1 Right shows the corresponding natural-weighted narrow-band PSF. This PSF is dominated by the radial diffraction spikes resulting from placing many antennas along the (straight) arms of the VLA and a broad pedestal due to the heavy concentration of short baselines.

The (u, v) coverage and beam for a single snapshot and frequency can be greatly improved by an extended observation and by bandwidth synthesis. However, bandwidth synthesis adds only a radial extent to each (u, v) point, which is of minimal help in removing radial features like those in Figure 1 Right. A 3 h synthesis with 5 m sampling and 2048 spectral channels between 2 and 4 GHz gives the PSF shown in Figure 2. This simulation kept only baselines longer than 200 λ and shorter than 500,000 λ at $\lambda = 0.1$ m, smoothed with an outer taper of 400,000 λ and an inner taper of 6,000 λ. Despite the extended "observation," the PSF is still dominated by radial features and large inner sidelobes. The skirts of the beam (Figure 2 right) have a "+" shape due to the predominantly north-south and east-west configuration of the outer antennas kept. It is difficult to define the resolution of such a PSF precisely, but in the following the resolution will be the size of an elliptical Gaussian fitted to the core of the beam.

[1] http://www.cv.nrao.edu/∼bcotton/Obit.html

IV. Limits to Dynamic Range

The effects probed in this memo are calibration errors, the presence of bright sources, and pixelization on images containing bright sources. In order to evaluate their effects on dynamic range, simulated data were generated and imaged. Simulation used Obit task UVSim which generates a (u, v) data set with specified frequencies and samples over a time range, adds a sky model, and adds Gaussian noise. In these tests 2048 channels in 16 "spectral windows" were simulated between 2 and 4 GHz.

The initial test used a sky model from a deep EVLA A-configuration observation at S band covering one primary beam area in a quiet portion of the sky; the brightest pixel is ~ 1.5 mJy beam^{-1}. Complex-gain calibration and antenna-pointing errors were simulated by generating a calibration table with various levels of Gaussian random noise for the real and imaginary parts of the gain for each spectral window and every 5 min for each antenna.

The next tests added much stronger point sources, both by themselves and added to the weaker source simulations. These tests also used the various corrupting calibration tables. Strong sources present a problem with pixelization. A source not exactly centered on a pixel can in principle be modeled with CLEAN by an infinite series of positive and negative components. In practice, the CLEAN support is much more limited and the defects in source model subtraction can leave significant artifacts. This problem and a solution are described in [5]. Pixelization can be dealt with fairly easily when using faceting for the "w term" correction: for each source brighter than a given threshold a facet is added in which the source is centered on the center pixel. This threshold is called the "autoCenter" flux density. When CLEAN reaches the autoCenter level, it reverts to CLEANing on the standard grid. Autocentering allows a more accurate subtraction of the CLEAN sky model. For these tests six point sources of flux densities 100, 30, 30, 10, 10, and 10 mJy were added at arbitrary positions and the tests covered a range autoCenter flux densities.

A. Simulated Data

In order to get a realistic sky model for testing, a real sky model derived from a deep EVLA image at S band (2–4 GHz) was used. Data were simulated for the strawman antenna configuration proposed for the ngVLA. 2048 spectral channels in 16 "Spectral windows" were used to cover 2–4 GHz, and time samples every 5 minutes covering 3 hours were made. The resolution of observations from which the sky model were determined ($0\,''.6$) is approximately that of the images from the simulated data. The Gaussian noise added to the visibilities resulted in simulated image noise levels about half that of the actual observations, which was $\sigma \approx 1\,\mu$Jy beam^{-1}.

B. Imaging

The ngVLA (u, v) coverage is both clumpy and centrally condensed owing to the large fraction of antennas in the central core and along the VLA arms. In order to approximate

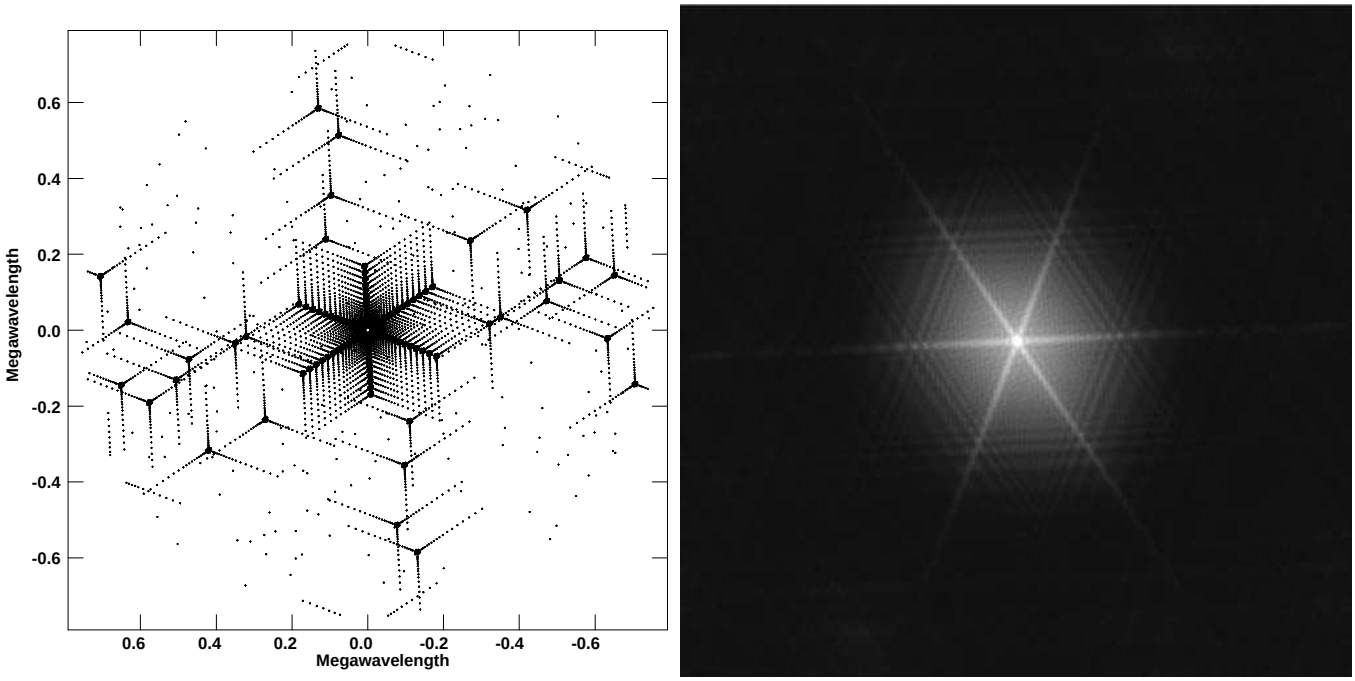

Fig. 1. Left: Snapshot narrowband (u, v) coverage; Right: The corresponding PSF displaying the $-5 \rightarrow 70\%$ intensity range.

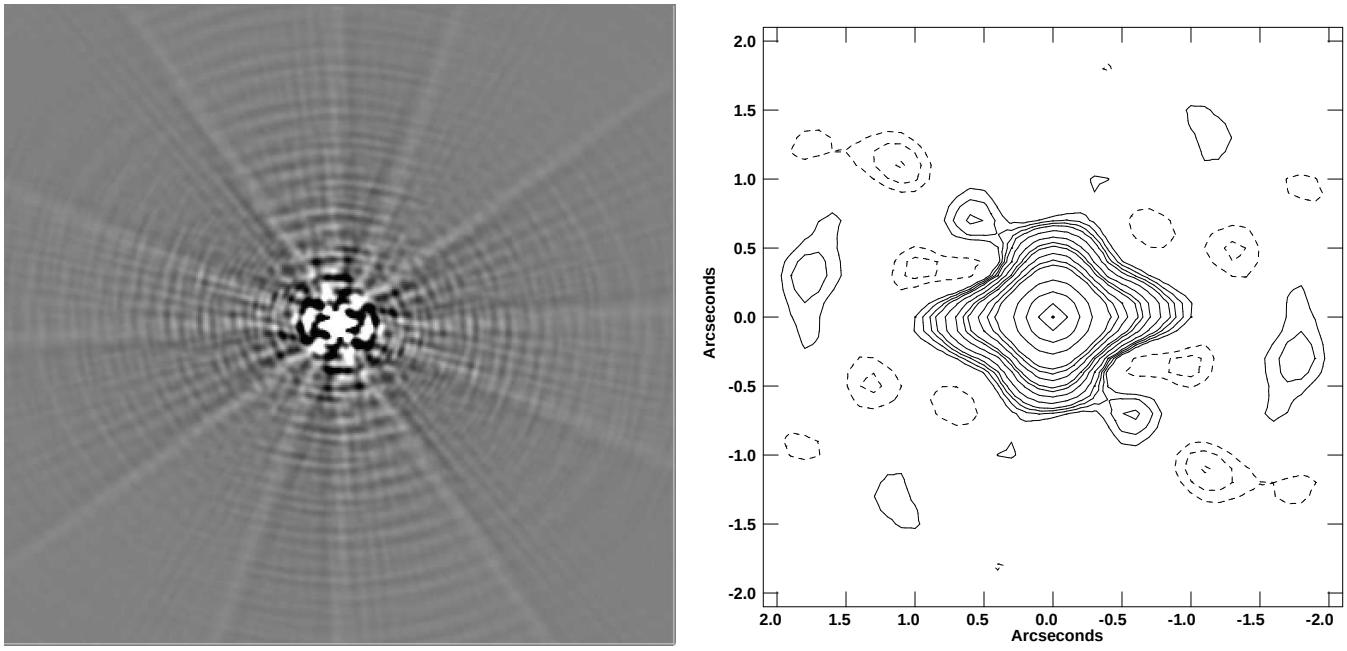

Fig. 2. ngVLA beam after 3 h and spanning 2-4 GHz, Left: grayscale ± 1%; Right: inner contours at -4,-3,-2,2,3,4,5,7,10,13,15,20,25,30,50,70,90, 99%.

the sky model resolution and get tolerable (if that) sidelobe levels, extensive weighting was needed. The Briggs Robust factor $R = -3$ (AIPS/Obit usage) used is biased strongly towards the uniform weight end of the robustness scale. Only baselines longer than 200 λ and shorter than 500,000 λ at $\lambda = 10$ cm were kept. A Gaussian outer taper of 400,000 λ was applied, and a Gaussian inner taper [6] of 6,000 λ with a minimum weight of 0.01 was applied to further downweight the massive core cluster of antennas. The Obit task MFImage used $0\,\farcs1$ cells to image the quiet-sky data (with or without the strong sources) out to a radius of 8.4 arcmin (10079×10079 pixels), and the strong-source-only data were imaged to a radius of 3.6 arcmin (3456×3456 pixels). Fifteen frequency bins were used to cover the frequency range and 55 "w" facets to cover the quiet-sky field. The depth of cleaning varied, but generally reached $\sim 20,000$ components and a depth of 1 to $3\,\mu\mathrm{Jy\ beam}^{-1}$ for images that included the quiet sky.

TABLE I
QUIET SKY TESTS

Corruption %	RMS μ Jy beam^{-1}	DR
0	0.451	3325
1	0.451	3325
2	0.452	3318
5	0.451	3325

Notes: Corruption is the percent Gaussian noise added to the real and imaginary parts of the calibration gain for each antenna, 5 minute interval and spectral window. The RMS pixel value fluctuation was measured in a box in the image which contained no "sources". DR is the dynamic range, the ratio of the brightest pixel value (1.5 mJy beam^{-1}) to the RMS.

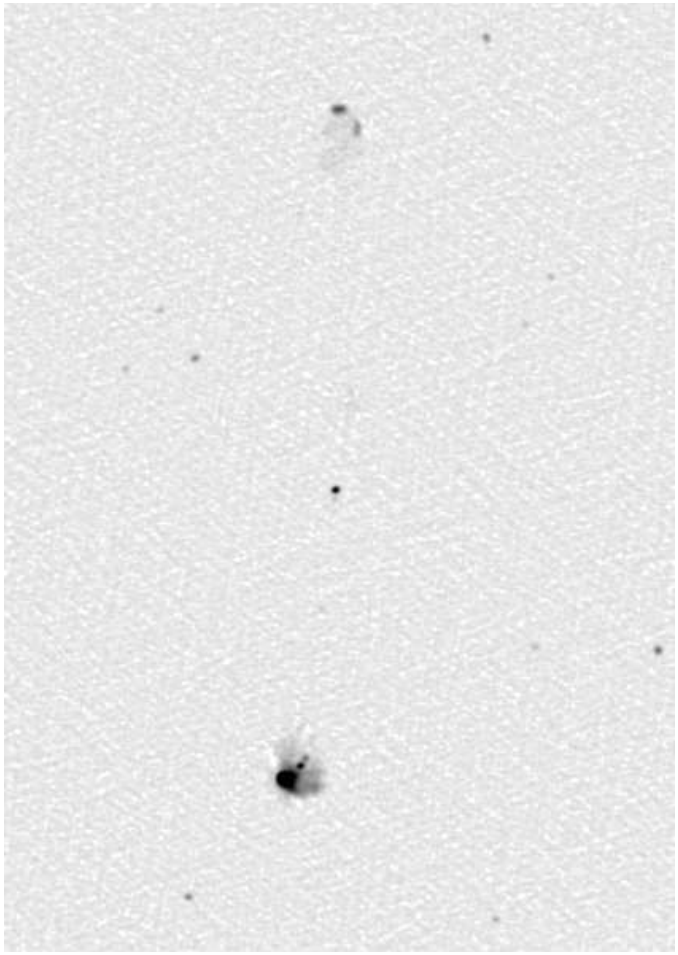

Fig. 3. Brightest portion of model field as negative grayscale with $\sqrt{\ }$ stretch, -1 to $100\,\mu$Jy beam^{-1}. In the observed image calibration artifacts were visible near the hotspot in the southern lobe.

C. Corrupted Quiet-Sky Tests

The quiet-sky data were imaged with gain corruptions of 0%, 1%, 2%, and 5%, and the results are shown in Table I. At the levels tested here, the corrupted calibration tables caused no harm. The region of the image containing the brightest emission is shown in Figure 3.

TABLE II
STRONG + QUIET TESTS

autoCenter mJy beam^{-1}	RMS μ Jy beam^{-1}	DR
∞	0.533	1.88×10^5
9	0.615	1.63×10^5
3	0.454	2.20×10^5
1	0.452	2.21×10^5

Notes: The RMS pixel value fluctuation was measured in a box in the image which contained no "sources". DR is the dynamic range, the ratio of the brightest pixel value (100 mJy beam^{-1}) to the RMS. No calibration corruptions were applied.

D. AutoCenter Tests

The utility of autoCentering to remove artifacts from bright sources was tested using data with uncorrupted calibration tables applied. The quiet-sky plus strong-source data were imaged with several values of the autoCenter threshold and a portion of the images near the 100 mJy source is shown in Figure 4. The top left panel shows the portion of the quiet sky, the top right has the strong source added without the autoCentering applied; strong artifacts are visible. The bottom panels show the results of autoCenter levels of 9 and 1 mJy beam^{-1}. At 1 mJy beam^{-1} the extended artifacts are essentially gone.

E. Strong-Source Plus Quiet-Sky Tests

The quiet-sky plus strong-source tests were run as described above. The RMS values in empty regions of the images were used to determine the dynamic range as a function of the autoCenter level, and the results are shown in Table II. Note the values in the lowest two autoCenter levels tested give values comparable to those in Table I for the quiet-sky tests. The autoCenter method appears to have largely removed the pixelization artifacts, and the addition of the stronger sources did not degrade the quality of the image. Note: this is with "perfect calibration".

F. Corrupted Strong Source Tests

Calibration errors will scatter power from a strong source and generate artifacts whose intensity decreases away from the strong source. A test data-set was generated with only the six stronger sources sampled every 5 min for three hours; these data were imaged with a variety of autoCenter levels and degrees of corruption in the calibration tables applied. The effects are characterized by the RMS derived from a histogram analysis of the central 2000×2000 pixels in the image. The test results are summarized in Table III. For the tests with no corruption added, the results are similar to those in Section IV-D; without autoCentering, there are significant artifacts but the use of the deeper autoCenter levels largely eliminated these (see also Figure 5). However, as the level of gain corruption increased, even autoCentering could not fully correct the images. The dynamic range of the 5% gain corruption is about one third of the uncorrupted image and autoCentering did little to improve the image.

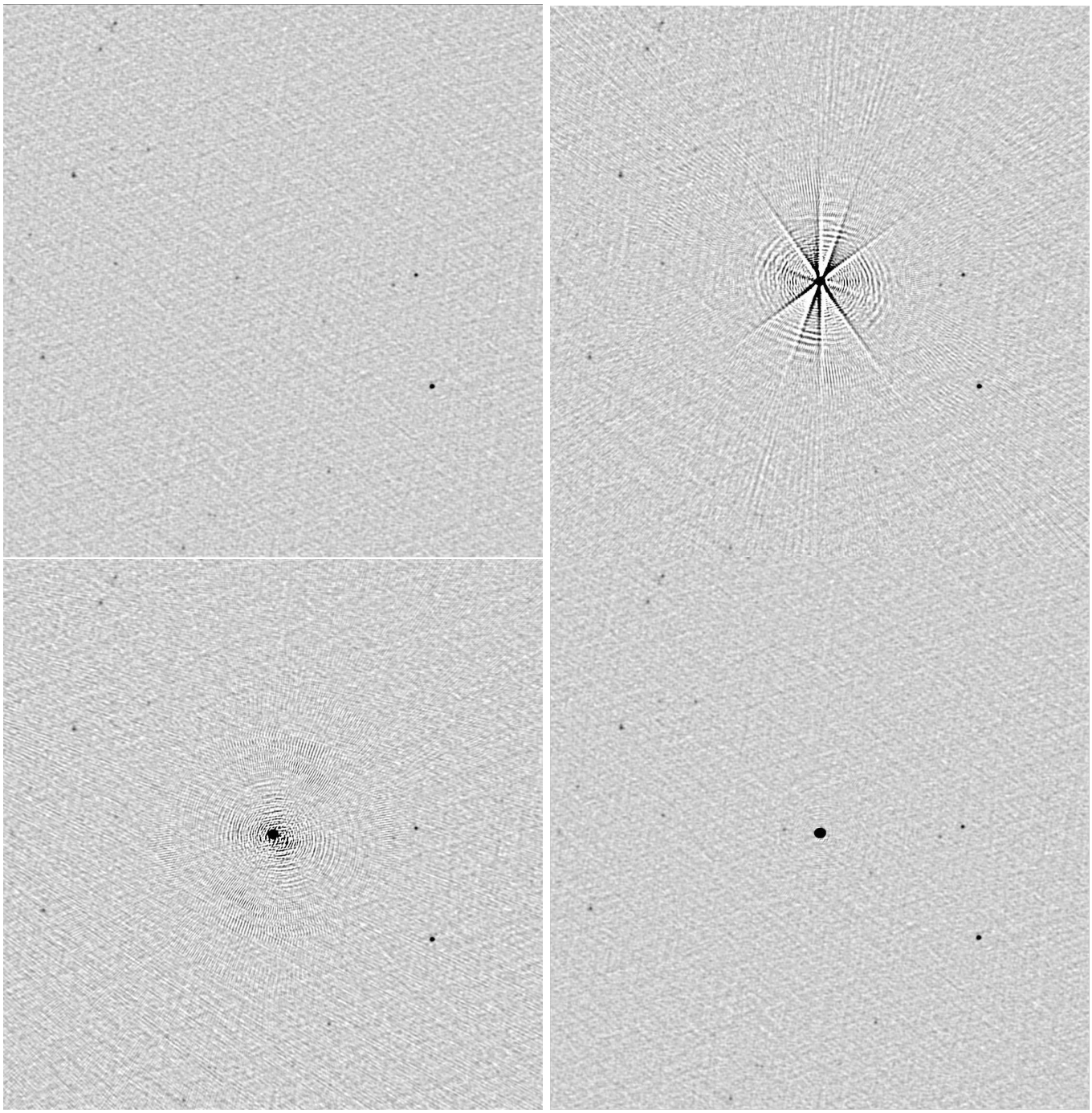

Fig. 4. Strawman configuration, strong source on model field as negative grayscale. top left: field before source added, top right: imaged with no autoCenter, bottom left: imaged with autoCenter= 9 $\mathrm{mJy\ beam^{-1}}$, bottom right: imaged with autoCenter= 1 $\mathrm{mJy\ beam^{-1}}$. All images shown with the same linear stretch, -1 to 5 $\mu\mathrm{Jy\ beam^{-1}}$.

The tests described above measured the general level of added noise from the scattered power from the strong sources. In general, the level of artifacts is much higher near the offending source than farther away. Figure 5 shows the region in the autoCenter 1 $\mathrm{mJy\ beam^{-1}}$ images near the 100 mJy source for the various degrees of corruption. The dynamic range in the immediate vicinity of strong sources is greatly reduced by imperfect calibration.

V. Dithered Antenna Distribution

In an attempt to improve the snapshot (u, v) coverage and beam a "dithered" version of the antenna layout was tested in which the locations of the antennas originally along the VLA arms were given random offsets from the arm. The snapshot (u, v) coverage and corresponding narrow-band beam are shown in Figure 6 for natural weighting including all baselines shorter than 500,000 λ at $\lambda = 10$ cm.

A 3 h synthesis using the dithered distribution including

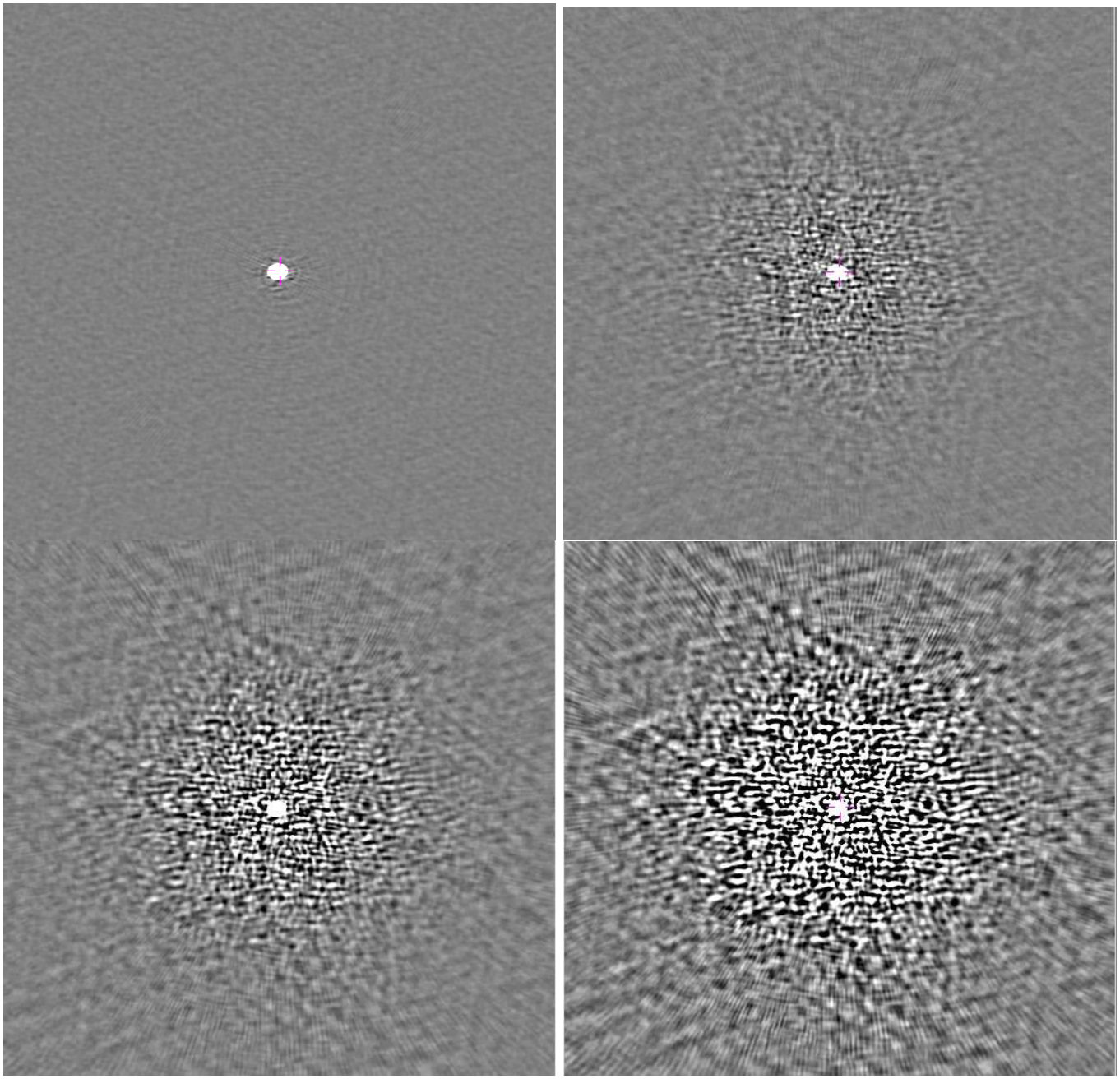

Fig. 5. Strawman configuration, strong source with various levels of corruption images using autoCenter 1 $\mathrm{mJy\ beam^{-1}}$. top left: No corruption, top right: 1% gain errors, bottom left: 2% gain errors, bottom right: 5% gain errors. All images shown with the same linear stretch, -10 to +10 μ $\mathrm{Jy\ beam^{-1}}$; the region shown is 76"×76".

only baselines longer than 200 λ and shorter than 500,000 λ at at $\lambda = 10$ cm, and with an outer taper of 400,000 λ and an inner taper of 6,000 λ, is shown in Figure 7.

VI. Triangular Antenna Distribution

A more aggressive modification of the ngVLA antenna configuration is to move the antennas originally on the arms of the VLA onto a set of concentric, curved Reuleaux triangles, an ngVLA configuration referred to here as the "triangular distribution." Reuleaux polygons have the same diameter in all directions to yield direction-independent resolution. Among Reuleaux polygons, Reuleaux triangles have the lowest degree of rotational symmetry, so antennas on a Reuleaux triangle sample the (u, v) plane most uniformly [7]. The snapshot (u, v) coverage and corresponding narrowband beam are given in Figure 10.

A 3 h wideband synthesis using the triangular distribution included only baselines longer than 200 λ and shorter than 500,000 λ at $\lambda = 10$ cm, and had an outer taper of 400,000 λ and an inner taper of 6,000 λ. This 3 h wideband synthesis beam is shown in Figure 11.

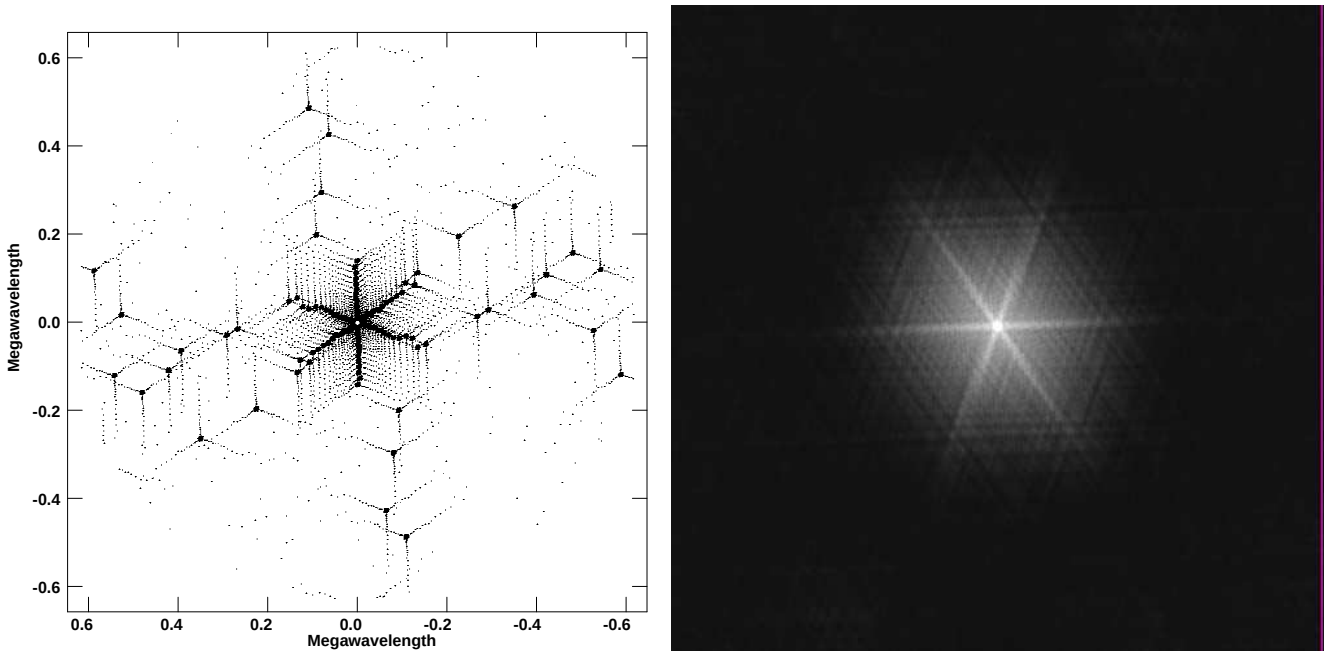

Fig. 6. Dithered configuration, Left: single channel snapshot (u, v) coverage; Right: corresponding PSF displaying -5 $\rightarrow$ 70%.

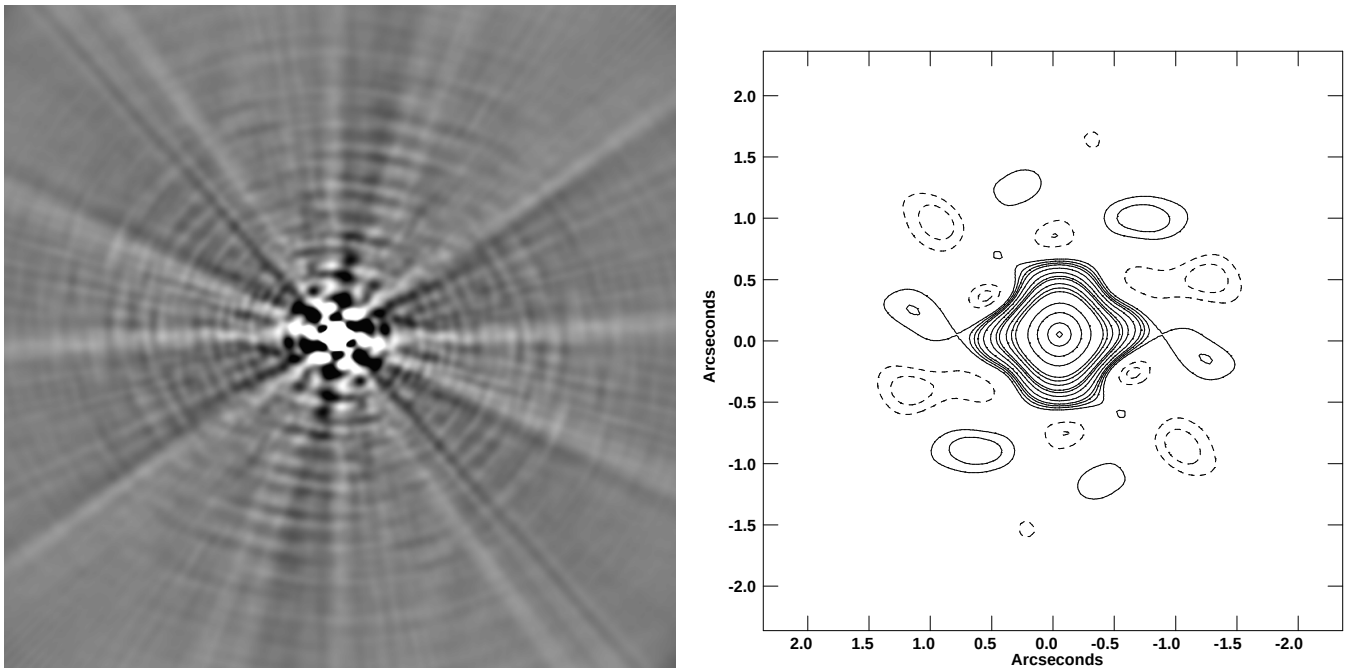

Fig. 7. Dithered configuration Three hour beam 2-4 GHz, Left: grayscale $\pm$ 1%; Right: inner contours at -4,-3,-2,2,3,4,5,7,10,13,15,20,25,30,50,70,90, 99%.

VII. Beam Analysis

In order to compare the synthesized beams of the ngVLA configurations with that of the EVLA, simulated data-sets were prepared with Gaussian noise but no sky model. These were then imaged with a variety of Briggs robust factors R. Positive values of Briggs R gave curious results. Note in these tests, the maximum ngVLA baseline is approximately twice that of the EVLA.

One measure of the quality of a synthesized beam is the fraction of the power in the main lobe of the synthesized response; larger sidelobes allow dynamic range limiting effects to scatter more power. To this end, a "main lobe efficiency" was derived. This was computed by the ratio of the sum of the absolute value of the beam image pixel intensities within an inner radius of the center to the sum within an outer radius. The inner radius was determined from the geometric mean of the major and minor axis FWHM of an elliptical Gaussian fitted to the main lobe. This gives more–or–less the size of the main lobe although the ngVLA beam is not particularly close to an elliptical Gaussian. The outer radius is arbitrary

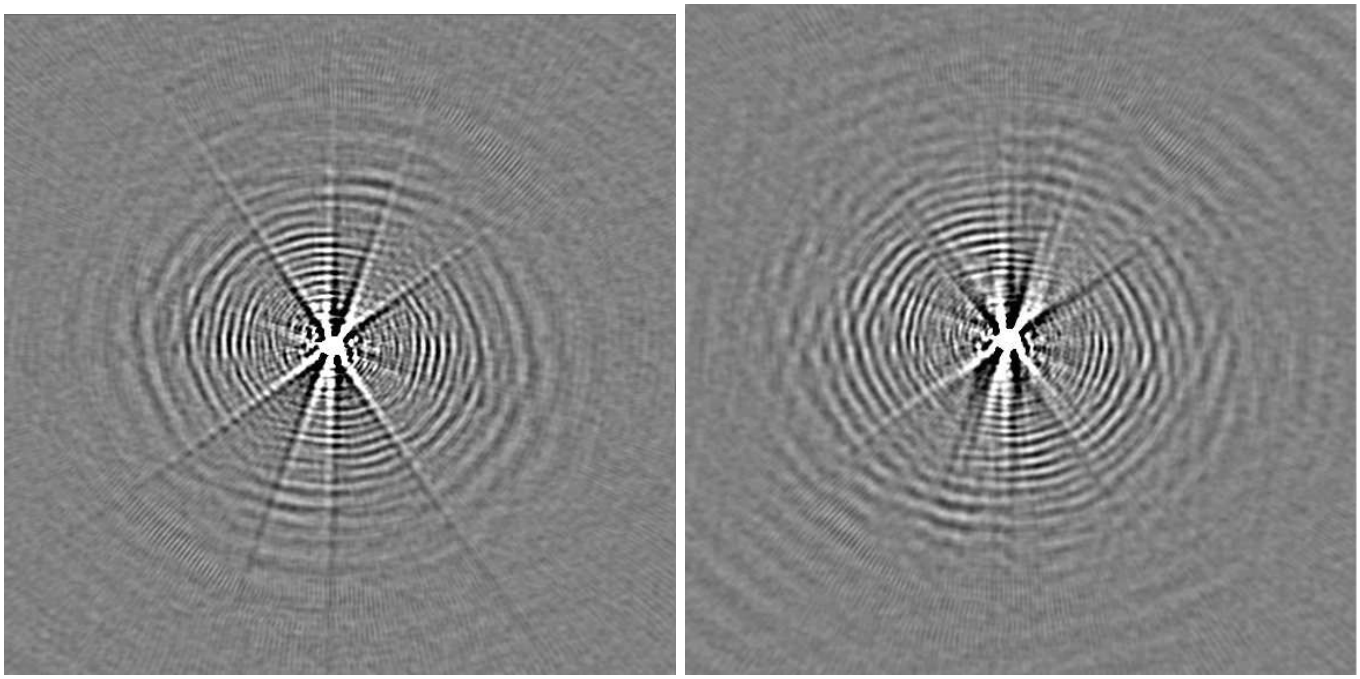

Fig. 8. 100 mJy point source imaged with no AutoCentering. Left: Strawman distribution; Right: Dithered distribution. All images shown with the same linear stretch, -10 to +10 μ Jy beam^{-1}; the region shown is 76"×76".

TABLE III
STRAWMAN STRONG SOURCE TESTS

Corruption %	autoCen mJy beam^{-1}	RMS μ Jy beam^{-1}	DR
0	∞	0.473	2.11×10^5
0	9	0.356	2.81×10^5
0	3	0.339	2.95×10^5
0	1	0.340	2.94×10^5
1	∞	0.506	1.98×10^5
1	9	0.420	2.38×10^5
1	3	0.410	2.44×10^5
1	1	0.410	2.44×10^5
2	∞	0.682	1.47×10^5
2	9	0.562	1.78×10^5
2	3	0.554	1.81×10^5
2	1	0.552	1.81×10^5
5	∞	1.118	0.89×10^5
5	9	1.096	0.91×10^5
5	3	1.100	0.91×10^5
5	1	1.099	0.91×10^5

Notes: Corruption is the percent Gaussian noise added to the real and imaginary parts of the calibration gain for each antenna, 5 minute interval and spectral window. The RMS pixel value fluctuation was determined from a histogram analysis of the central 2000×2000 pixels in the image. DR is the dynamic range or the ratio of the brightest pixel value to the RMS.

TABLE IV
DITHERED DIST: STRONG SOURCE TESTS

Corruption %	autoCen mJy beam^{-1}	RMS μ Jy beam^{-1}	DR
0	1	0.335	2.99×10^5
1	1	0.412	2.42×10^5
2	1	0.566	1.77×10^5
5	1	1.137	0.88×10^5

Notes: Corruption is the percent Gaussian noise added to the real and imaginary parts of the calibration gain for each antenna, 5 minute interval and spectral window. The RMS pixel value fluctuation was determined from a histogram analysis of the central 2000×2000 pixels in the image. DR is the dynamic range or the ratio of the brightest pixel value to the RMS.

TABLE V
TRIANGULAR DIST: STRONG SOURCE TESTS

Corruption %	autoCen mJy beam^{-1}	RMS μ Jy beam^{-1}	DR
0	1	0.261	3.83×10^5
1	1	0.315	3.17×10^5
2	1	0.419	2.39×10^5
5	1	0.827	1.21×10^5

Notes: Corruption is the percent Gaussian noise added to the real and imaginary parts of the calibration gain for each antenna, 5 minute interval and spectral window. The RMS pixel value fluctuation was determined from a histogram analysis of the central 2000×2000 pixels in the image. DR is the dynamic range or the ratio of the brightest pixel value to the RMS.

as the sum of the absolute pixel values continues to increase outward but an arbitrary value of 10 times the inner radius was chosen to allow comparisons. For some of the ngVLA tests this outer radius was larger than the size of the beam image and the main lobe efficiency could not be determined.

A. ngVLA strawman

The data for the ngVLA strawman beam tests were generated using 5 minute sampling over a period of 3 hours with 2048 channels covering 2–4 GHz and using the proposed ngVLA configuration. Baselines were limited to the range 0 to 500,000 λ at 2 GHz (0–75 km), and 10 mJy Gaussian random noise was added to the real and imaginary parts of each correlation but without a sky model. Imaging used

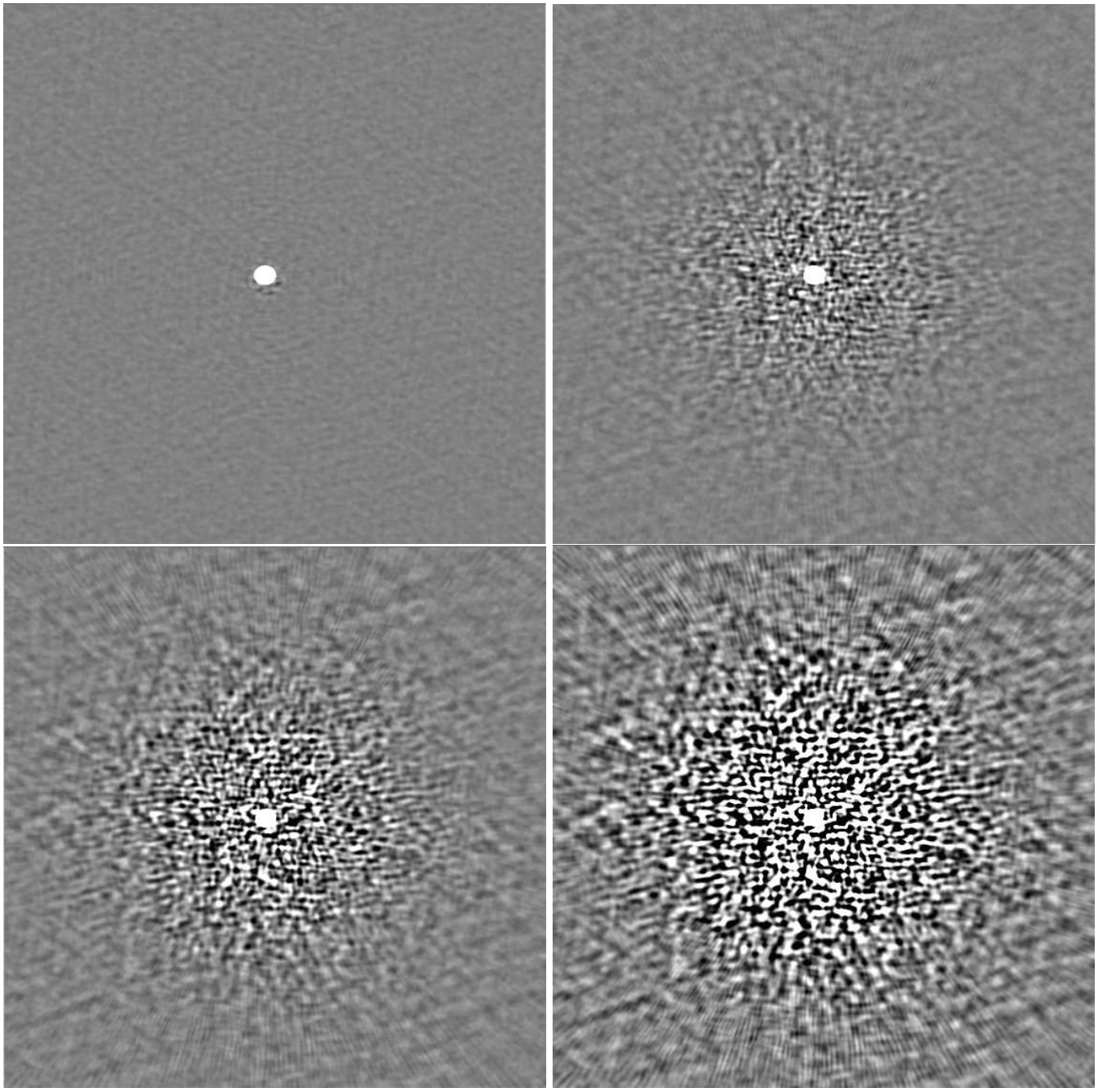

Fig. 9. Dithered distribution: Strong 100 mJy source with various levels of corruption, imaged using autoCenter 1 $\mathrm{mJy\ beam^{-1}}$. top left: No corruption, top right: 1% gain errors, bottom left: 2% gain errors, bottom right: 5% gain errors. All images shown with the same linear stretch, -10 to +10 μ $\mathrm{Jy\ beam^{-1}}$; the region shown is 76"×76".

a fixed image size of 1024×1024 pixels $0\,\farcs035$ on a side. Simple imaging tests were performed with no inner or outer tapers or additional limits on the (u, v) range; the results are summarized in Table VI. For comparison, the imaging parameters used for the dynamic range tests had a main lobe efficiency of 0.479, a Briggs factor of 2.16, a beam size of $0\,\farcs50$ and an RMS of 0.341 μ $\mathrm{Jy\ beam^{-1}}$.

B. EVLA

The data for the EVLA beam tests were generated using 1 minute sampling over a period of 3 hours with 2048 channels covering 2–4 GHz and using a 27 antenna VLA "A" configuration. 10 mJy Gaussian random noise was added to the real and imaginary parts of each correlation but without a sky model. Imaging used a fixed image size of 512×512 pixels of 0.1". Simple imaging tests were performed with no inner or outer tapers or additional limits on the (u, v) range; the results are summarized in Table VII.

C. Dithered Distribution

The data for the dithered distribution beam tests was generated using 5 minute sampling over a period of 3 hours

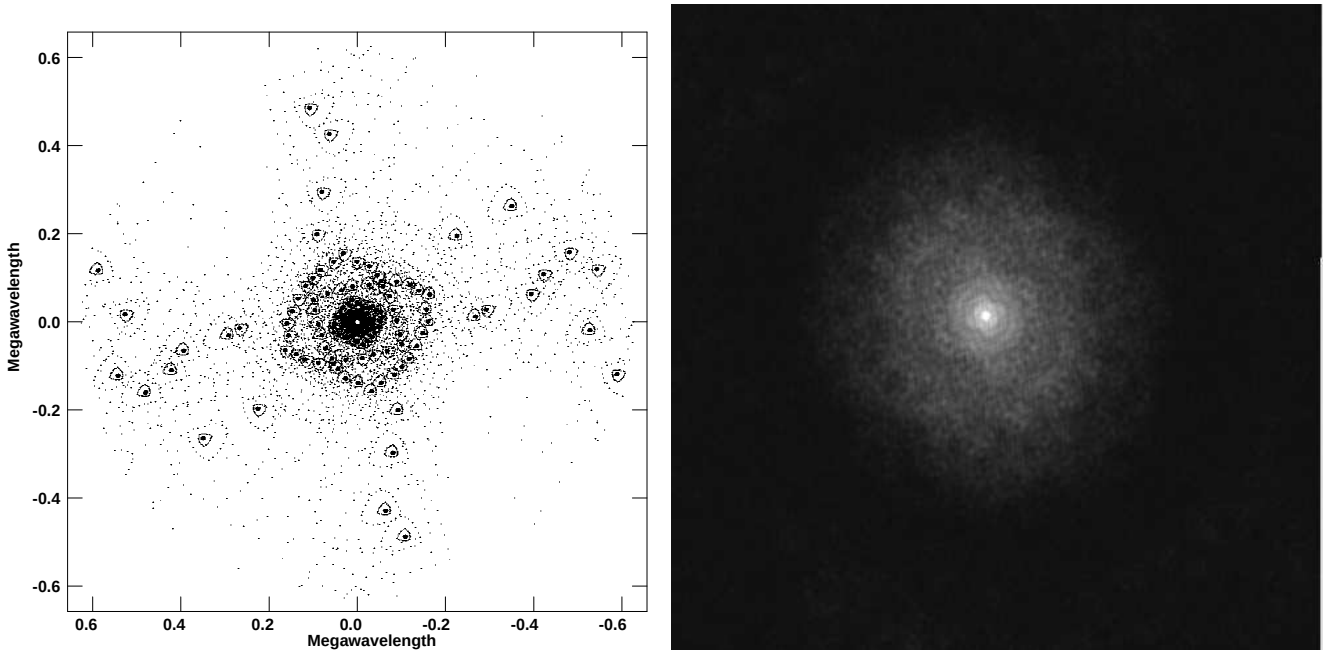

Fig. 10. Triangular configuration Left: Snapshot single channel (u, v) coverage; Right: corresponding PSF displaying -5 → 70%.

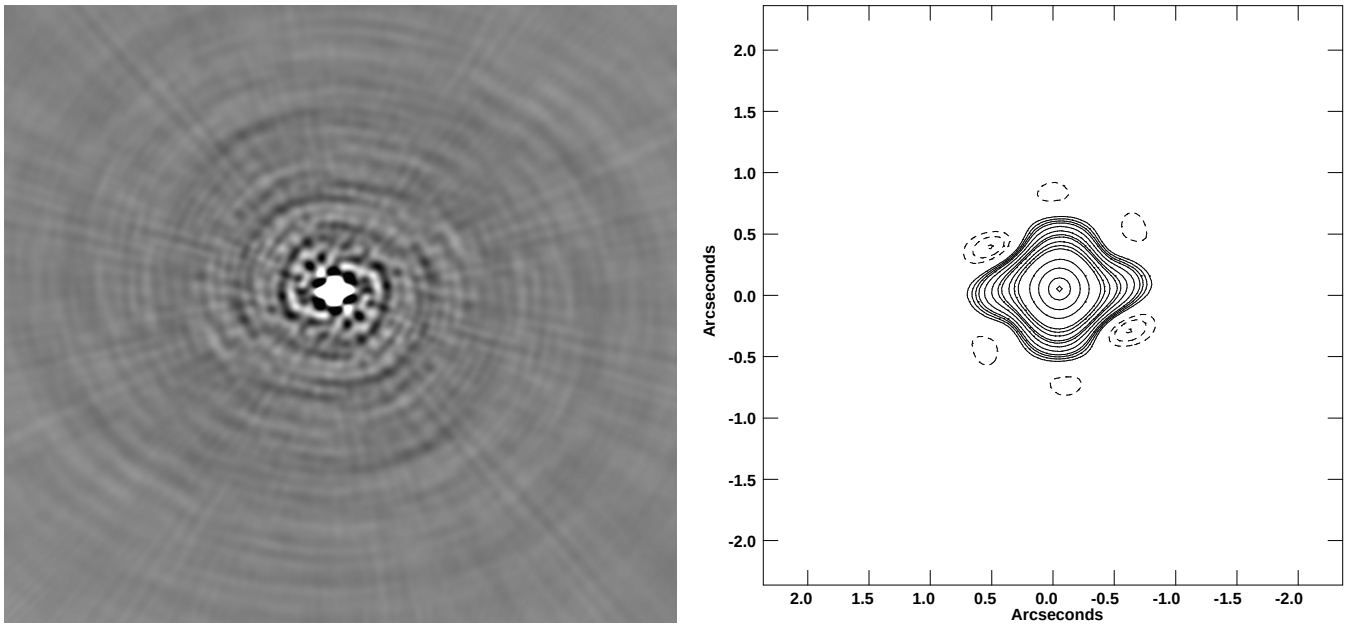

Fig. 11. Triangular configuration, 3 h synthesis, 2–4 GHz, Left: grayscale ± 1%; Right: inner contours at -4,-3,-2,2,3,4,5,7,10,13,15,20,25,30,50,70,90, 99%.

with 2048 channels covering 2-4 GHz. 10 mJy Gaussian random noise was added to the real and imaginary parts of each correlation but without a sky model. Imaging used a fixed image size of 1024×1024 pixels $0\,\farcs035$ on a side. Simple imaging tests were performed with no inner or outer tapers or additional limits on the (u, v) range; the results are summarized in Table IX. For reference, the robust and tapers used for imaging (with robust $R = -3$, only baselines longer than 200 λ and shorter than 500,000 λ at $\lambda = 10$ cm, with an outer taper of 400,000 λ and an inner taper of 6,000 λ) gives a beam size of $0\,\farcs50$, a Briggs factor of 2.14, an RMS of 0.336 μ Jy beam^{-1} and a main lobe efficiency of 0.482. The synthesized beam is given in Figure 7.

D. Triangular Distribution

The data for the triangular distribution beam tests was generated using 5 minute sampling over a period of 3 hours with 2048 channels covering 2–4 GHz and using the triangular configuration. 10 mJy Gaussian random noise was added to the real and imaginary parts of each correlation but without a sky model. Imaging used a fixed image size of 1024×1024 pixels $0\,\farcs035$ on a side. Simple imaging tests were performed with no inner or outer tapers or additional limits on the (u, v) range; the results are summarized in Table IX. For reference,

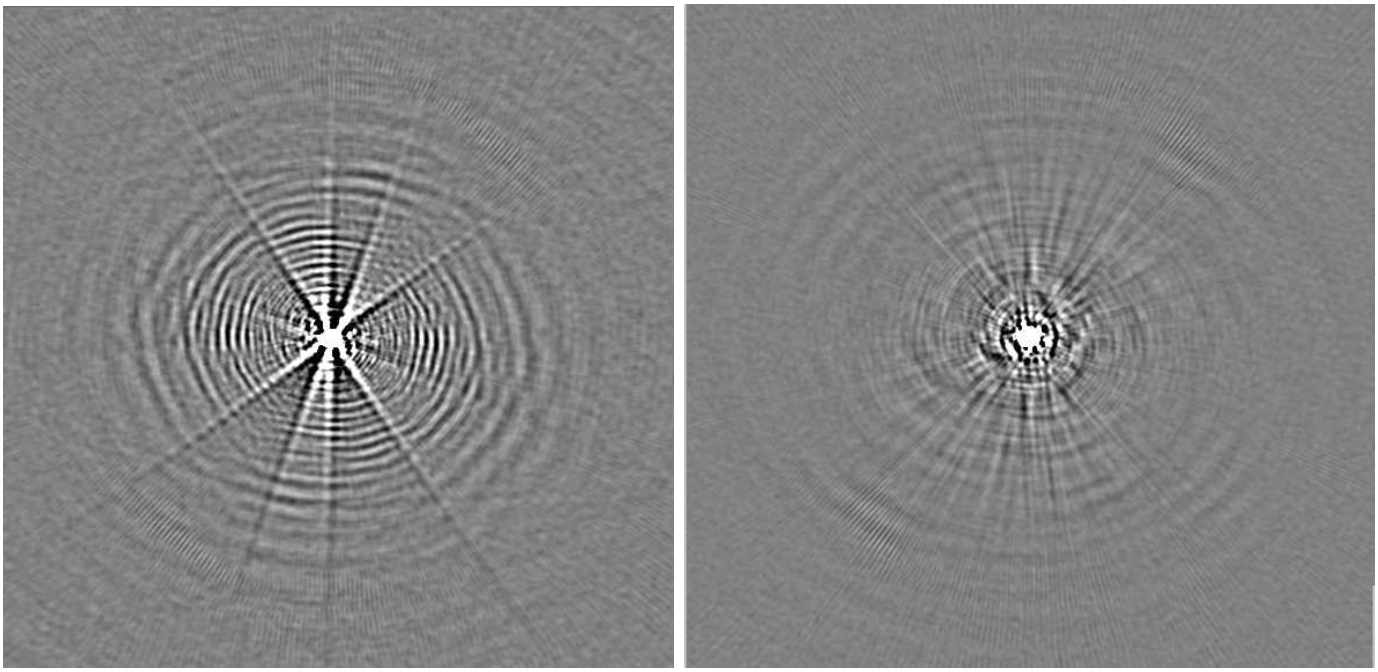

Fig. 12. 100 mJy point source imaged with no AutoCentering. Left: Strawman distribution; Right: Triangular distribution. All images shown with the same linear stretch, -10 to +10 μ Jy beam^{-1}; the region shown is 76"×76".

TABLE VI
SIMPLE STRAWMAN WEIGHTING TESTS

Weight	Beam "	RMS μ Jy beam^{-1}	Factor	Eff
Uni.	0.16	0.704	16.8	0.523
R=-5	0.19	0.545	5.88	0.557
R=-4	0.19	0,401	3.18	0.447
R=-3	0.30	0.314	2.18	0.361
R=-2	0.58	0.262	1.70	0.277
R=-1	0.92	0.224	1.38	0.216
R=0	1.36	0.201	1.21	0.164
Nat.	2.54	0.155	1.0	*

Notes: Weight is Uniform, Natural or Briggs robust (R=?), Beam is the geometric mean of the major and minor fitted beam size, RMS is the RMS in the image, Factor is the Briggs noise factor, Eff is the main lobe efficiency, * indicates that the beam image wasn't large enough to determine efficiency.

TABLE VII
SIMPLE EVLA WEIGHTING TESTS

Weight	Beam "	RMS μ Jy beam^{-1}	Factor	Eff
Uni.	0.49	0.675	5.32	0.655
R=-5	0.49	0.675	5.23	0.654
R=-4	0.49	0.673	4.82	0.655
R=-3	0.49	0.665	4.15	0.658
R=-2	0.49	0.638	3.06	0.680
R=-1	0.54	0.569	1.81	0.730
R=0	0.69	0.519	1.21	0.578
R=1	1.03	0.527	1.03	0.330
Nat.	1.42	0.562	1.00	0.242

Notes: Weight is Uniform, Natural or Briggs robust (R=?), Beam is the geometric mean of the major and minor fitted beam size, RMS is the RMS in the image, Factor is the Briggs noise factor, Eff is the main lobe efficiency.

TABLE VIII
SIMPLE DITHERED WEIGHTING TESTS

Weight	Beam "	RMS μ Jy beam^{-1}	Factor	Eff
Uni.	0.16	0.701	16.7	0.522
R=-5	0.16	0.548	5.89	0.555
R=-4	0.20	0.399	3.18	0.449
R=-3	0.30	0.313	2.18	0.356
R=-2	0.54	0.263	1.70	0.289
R=-1	0.92	0.229	1.38	0.224
R=0	1.36	0.209	1.21	0.163
Nat.	2.68	0.163	1.00	0.577*

Notes: Weight is Uniform, Natural or Briggs robust (R=?), Beam is the geometric mean of the major and minor fitted beam size, RMS is the RMS in the image, Factor is the Briggs noise factor, Eff is the main lobe efficiency, * indicates that the beam image was't large enough to determine.

the robust and tapers used for imaging (with Robust $R = -3$, only baselines longer than 200 λ and shorter than 500,000 λ at $\lambda = 10$ cm, with an outer taper of 400,000 λ and an inner taper of 6,000 λ) gives a beam size of $0\farcs47$, a Briggs factor of 1.94, an RMS of 0.273 μ Jy beam^{-1} and a main lobe efficiency of 0.682. The synthesized beam is given in Figure 11.

VIII. CONFIGURATION NOISE PENALTY

An array of N antennas has $n_{\rm b} = N(N-1)/2$ independent baselines. If the antennas are identical and the baselines are assigned weights w_i during imaging, then the image signal from a point source is proportional to

$$\sum_{i=1}^{n_{\rm b}} w_i \ , \qquad (1)$$

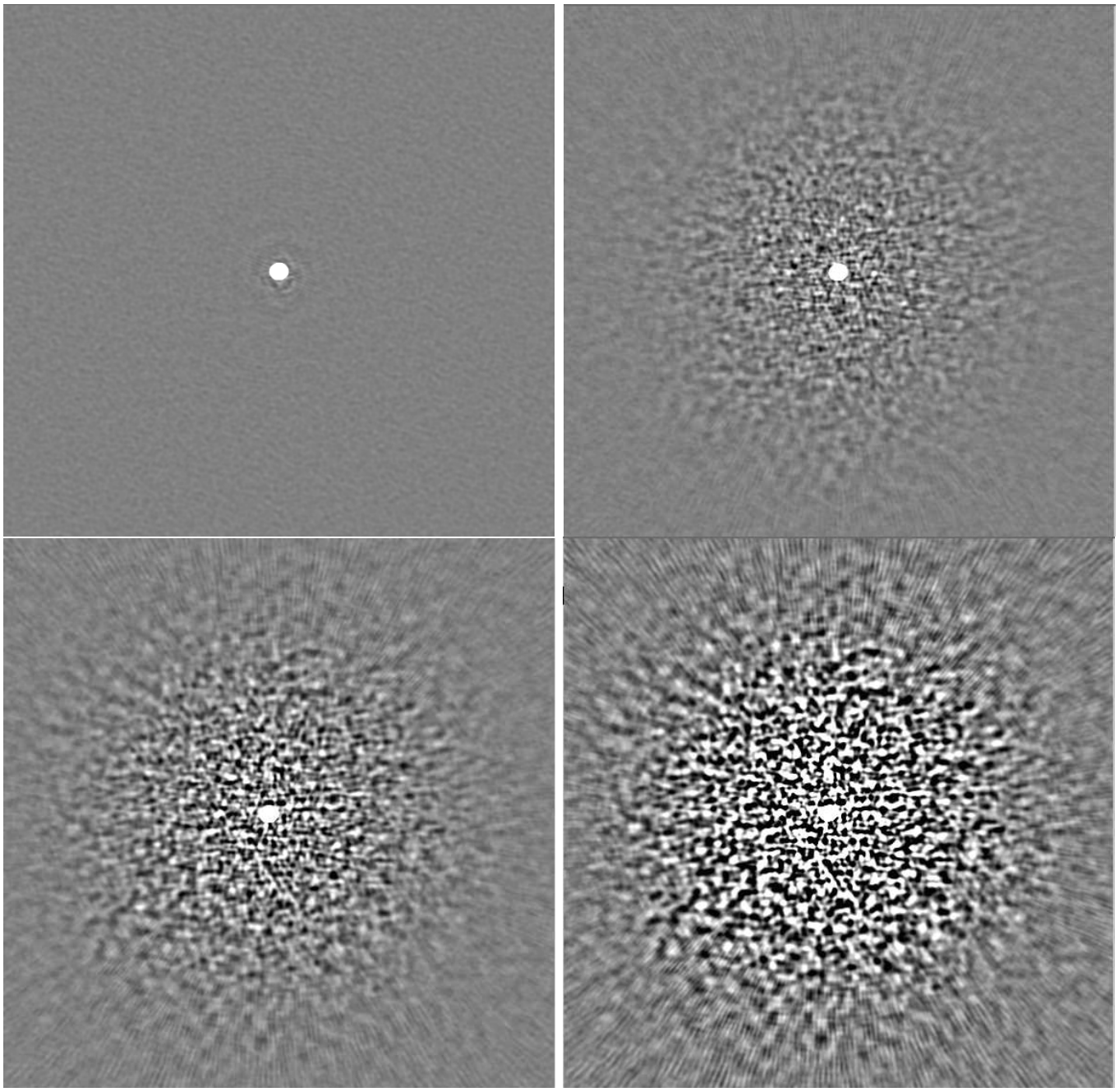

Fig. 13. Triangular distribution: Strong 100 mJy source with various levels of corruption, imaged using autoCenter 1 $\mathrm{mJy\ beam^{-1}}$. top left: No corruption, top right: 1% gain errors, bottom left: 2% gain errors, bottom right: 5% gain errors. All images shown with the same linear stretch, -10 to +10 μ $\mathrm{Jy\ beam^{-1}}$; the region shown is 76"×76".

the rms noise is proportional to

$$\left(\sum_{i=1}^{n_\mathrm{b}} w_i^2\right)^{1/2}, \tag{2}$$

and the signal-to-noise ratio is proportional to

$$\sum_{i=1}^{n_\mathrm{b}} w_i \Bigg/ \left(\sum_{i=1}^{n_\mathrm{b}} w_i^2\right)^{1/2}. \tag{3}$$

In the case of natural weighting (equal w_i), the signal-to-noise ratio is proportional to $\sqrt{n_\mathrm{b}}$. Natural weighting maximizes the signal-to-noise ratio but usually degrades the synthesized point-spread function, particularly for centrally concentrated arrays. Any other weighting scheme (e.g., tapering, Briggs weighting) designed to improve the dirty beam divides the signal-to-noise ratio by the factor

$$F = \left(n_\mathrm{b} \sum_{i=1}^{n_\mathrm{b}} w_i^2\right)^{1/2} \Bigg/ \sum_{i=1}^{n_\mathrm{b}} w_i\ . \tag{4}$$

In a completely reconfigurable array, the antennas could be moved to yield a dirty beam with the desired beamwidth (or surface-brightness sensitivity, which is inversely proportional

TABLE IX
SIMPLE TRIANGULAR WEIGHTING TESTS

Weight	Beam ″	RMS μ Jy beam^{-1}	Factor	Eff
Uni.	0.16	0.663	16.5	0.493
R=-5	0.16	0.542	6.50	0.523
R=-4	0.19	0.399	3.44	0.491
R=-3	0.27	0.269	2.24	0.408
R=-2	0.49	0.233	1.64	0.497
R=-1	0.83	0.211	1.33	0.403
R=0	1.23	0.200	1.16	0.270
Nat.	2.17	0.178	1.00	0.861 *

Notes: Weight is Uniform, Natural or Briggs robust (R=?), Beam is the geometric mean of the major and minor fitted beam size, RMS is the RMS in the image, Factor is the Briggs noise factor, Eff is the main lobe efficiency, * indicates that the beam image wasn't large enough to determine.

to the beam solid angle) and low sidelobes with nearly natural weighting. In a fixed configuration, the weights needed to produce the desired beamwidth and low sidelobes will divide the point-source signal-to-noise ratio by F; that is, the factor F represents the configuration noise penalty. As written, Equation 4 applies to one visibility per baseline. However, it is easily generalized to $n_{\rm s}$ time samples and $n_{\rm f}$ frequency channels per baseline: simply replace all $n_{\rm b}$ by $n = n_{\rm b}n_{\rm s}n_{\rm f}$.

In the present ngVLA examples, $N = 214$, $n_{\rm b} = 22791$, $n_{\rm s} = 34$, $n_{\rm f} = 2048$, and $n = n_{\rm b}n_{\rm s}n_{\rm f} = 1.587 \times 10^9$. The configuration weights are

$$\sum_{i=1}^{n} w_i = 1.711 \times 10^{11} \quad \text{and} \quad \sum_{i=1}^{n} w_i^2 = 1.185 \times 10^{14}$$
$$\sum_{i=1}^{n} w_i = 1.721 \times 10^{11} \quad \text{and} \quad \sum_{i=1}^{n} w_i^2 = 1.172 \times 10^{14}$$
$$\sum_{i=1}^{n} w_i = 1.422 \times 10^{11} \quad \text{and} \quad \sum_{i=1}^{n} w_i^2 = 6.409 \times 10^{13}$$

for the strawman, dithered, and triangle configurations, respectively. The corresponding noise penalties for the imaging parameters used in previous sections (Robust $R = -3$, inner and outer tapers) are

$$F = \frac{(1.587 \times 10^9 \cdot 1.185 \times 10^{14})^{1/2}}{1.711 \times 10^{11}} \approx 2.53 \quad (5)$$
$$F = \frac{(1.587 \times 10^9 \cdot 1.172 \times 10^{14})^{1/2}}{1.721 \times 10^{11}} \approx 2.51 \quad (6)$$
$$F = \frac{(1.587 \times 10^9 \cdot 6.409 \times 10^{13})^{1/2}}{1.422 \times 10^{11}} \approx 2.24 \quad (7)$$

for the strawman, dithered, and triangle configurations, respectively.

It is worth noting that this analysis is similar to the estimate given in Briggs weighting of the point-source sensitivity loss due to weighting except that the above analysis assumes that all data have equal "noise" weights and includes the array baselines that were eliminated by restrictions on the (u, v) range — effectively given 0 weight. Thus, the "Factor" columns given in the "Simple Weighting Tests" in section VII should be increased by ≈10% to include the discarded data.

IX. DISCUSSION

The proposed ngVLA or MeerKAT are fixed arrays intended to make images with a wide range of resolutions at any wavelength. However, their baseline lengths do not have a smooth power-law distribution. A sizable fraction of the total collecting area is in a central antenna cluster which has very high brightness-temperature sensitivity but low angular resolution. A set of "remote" antennas far outside to the central cluster provides high angular resolution. The natural (u, v) coverage/PSF shape of such arrays when used for imaging is intrinsically poor. The bulk of the sensitivity is in baselines which are either very short or very clustered around the many baselines from each remote antenna to the central cluster. The remote-to-remote baselines which provide the bulk of the (u, v) coverage have very low weight compared to the remote–central cluster set of baselines. Consequently the natural synthesized beam has a very broad pedestal from the very short baselines with small scale structure on top; see Figures 1, 6 and 10.

More nearly uniform weighting of the data can improve the imaging qualities of such an array, but at a significant cost in sensitivity. This procedure down-weights the densely sampled portions of the (u, v) plane and reduces the sensitivity of the central cluster. Briggs weighting allows a less harsh down-weighting of the overpopulated regions of (u, v) space and better imaging with less sensitivity loss. Also, in the tests presented here, adding an inner taper[6] which gradually down-weights the shortest baselines to an outer taper further improves the imaging quality. See Figures 2, 7 and 11.

A number of tests were presented evaluating the effects of the strawman proposed ngVLA antenna configuration as well as several modifications on the dynamic range achievable at $\sim 0\,\farcs5$ resolution at 3 GHz. Tests consisted of imaging wideband (2048 channels 2–4 GHz) simulated data with a temporal sampling every 5 minutes of a 3 hour observation. For tests involving faint sources, a sky model derived for a deep A-configuration S-band EVLA observation was used; stronger point sources, up to 100 mJy, were also added. The effects of calibration and pointing errors were simulated by "corrupting" the observations using a calibration table with Gaussian random errors at several levels. For the faint "quiet" sky with only faint sources, none of the corrupting calibrations degraded the ≈ 3300:1 dynamic range of the strawman configuration.

Tests using the stronger sources showed that the triangular configuration, as tested, had a limiting dynamic range of $\approx 4.0 \times 10^5$; the other configurations had a dynamic range about 30% worse. The stronger source images showed an additional "pixelization" error which results from strong, unresolved sources not centered on a pixel. The autoCentering feature of Obit Imaging tasks almost completely removes this error; see Figure 4.

Tests of strong-source data corrupted by 0, 1, 2 and 5% calibration errors reveal an increasing degradation of the dynamic range; at the highest level of corruption tested, the autoCentering showed limited improvement in the image quality.

The different proposed ngVLA configurations tested showed varying sensitivity to the dynamic-range limiting effects. The strawman configuration has remote antennas at a distance of several to several tens of km from the core along the arms of the current VLA. Like the EVLA, this configuration has poor snapshot performance due to the radial diffraction spikes in the PSF caused by the straight arms. This radial (u, v) coverage is not improved by bandwidth synthesis, which effectively extends each (u, v) point in the radial direction. Even for the extended observations tested here, radial features in VLA the beam pattern persist. Furthermore, the dominant north-south and east-west offsets of the ngVLA antennas beyond the ends of the VLA arms produce a "+" shaped PSF which persists even with the extended observations.

The two modifications of the strawman configuration tested were the "dithered" configuration in which antennas along the VLA arms were offset from the arms by a random amount and the "triangular" configuration in which the antennas at several to several 10s of km were arranged in a concentric set of curved triangles. In the strong-source dynamic range tests (Tables III, IV and V) for the most aggressive autoCentering the triangular configuration gave consistently 30% higher dynamic range for the various levels of corruption applied. The dithered configuration was not significantly better than the strawman.

A different way of evaluating the quality of an antenna configuration is by the fraction of the power in the main lobe of its PSF. The more power outside the main lobe, the easier it is for dynamic range reducing effects to scatter power. In principle, this can be evaluated by the ratio of the sum of the absolute value of all pixels in the derived dirty beam inside and outside of the main lobe. The practical difficulties are that 1) the main lobe of the derived PSF are of odd shape so "in" and "out" of the main lobe is not easily defined and 2) nonzero power in the PSF extends to an arbitrary distance so an outer limit need be adopted. For this purpose, the geometric mean of the FWHM of major and minor axes of an elliptical Gaussian fitted to the central core is taken as the extent of the main lobe and 10 times this value as the outer limit of the summation. Imaging used a fixed image (and beam) and pixel size to allow better comparison. A range of robust factors, including uniform and natural weighting for the ngVLA configurations as well as for the current VLA were tested. The values are given in Tables VI, VII, VIII and IX. In addition to the main lobe efficiency, these tables give the beam size, Briggs noise factor and the derived image RMS.

By the beam efficiency tests there were not strong differences among the ngVLA configurations shown in Tables VI, VIII, and IX, but all were significantly worse that the similar measures of the EVLA (Table VII). The main lobe efficiencies of the ngVLA configurations increase towards more uniform weighting, with increasing Briggs noise factor, but are systematically below the corresponding resolution values for the EVLA.

These tests used only the basic (u, v) range 0-500,000 λ and robust weighting. The imaging tests used additional inner and outer tapers and gave better main lobe efficiency than the robust-only tests. The triangular distribution using the inner and outer tapers had a a main lobe efficiency comparable with the EVLA's. Further gains may well be had.

An important consideration for multi-resolution, centrally condensed fixed arrays such as MeerKAT or ngVLA is an estimate of the sensitivity loss suffered by observations processed in a given way and for a given purpose relative to an array of the same collecting area optimally designed for that observation. The science case discussed in this memo is deep surveys of mostly unresolved sources. Section VIII gives an analysis of the several ngVLA array configurations as imaged in the tests presented in previous sections and concludes that the sensitivity loss factors are 2.53, 2.51, and 2.24 for the strawman, dithered, and triangle configurations.

There is a further complication with a PSF as far from an elliptical Gaussian as are those for the ngVLA configurations. The current practice is to "restore" the CLEAN components to the residuals using an elliptical Gaussian fitted to the PSF without scaling either the components or the residuals. This is appropriate when the units (in Jy per beam solid angle) of the two parts of the restored image are the same. This requires that the area of the CLEAN restoring beam and the dirty beam (units of the residuals) are approximately equal. With the poor ngVLA beams we found, this may not be the case, and scaling of either the residuals or CLEAN components may be needed.

This analysis should be extended to other science use cases involving more extended sources and other angular resolutions.

REFERENCES

[1] E. Selina, R. & Murphy, *ngVLA Memo*, vol. 17, 2017.
[2] A. e. a. Bolatto, *ngVLA Memo*, vol. 19, 2017.
[3] C. L. Carilli, *ngVLA Memo*, vol. 16, 2017.
[4] W. D. Cotton, "Obit: A Development Environment for Astronomical Algorithms," *PASP*, vol. 120, pp. 439–448, 2008.
[5] W. D. Cotton and J. M. Uson, "Pixelization and Dynamic Range in Radio Interferometry," *A & A*, vol. 490, pp. 455–460, 2008.
[6] W. D. Cotton, "Inner UV Taper Weighting for Synthesis Imaging," *Obit Development Memo Series*, vol. 50, pp. 1–9, 2017.
[7] E. Keto, *ApJ*, vol. 475, p. 843, 1997.